Inorganic Chemistry

Article

pubs.acs.org/IC

Localization of Oxygen Interstitials in $CeSrGa_3O_{7+\delta}$ Melilite

Jungu Xu,[†,‡] Xiaojun Kuang,*[,†,‡] Emmanuel Véron,[§,⊗] Mathieu Allix,[§,⊗] Matthew R. Suchomel,[∥] Florence Porcher,[⊥] Chaolun Liang,[#] Fengjuan Pan,[†] and Mingmei Wu*[,†]

[†]MOE Key Laboratory of Bioinorganic and Synthetic Chemistry, State Key Laboratory of Optoelectronic Materials and Technologies, School of Chemistry and Chemical Engineering, Sun Yat-Sen University, Guangzhou 510275, P. R. China

[‡]Guangxi Ministry-Province Jointly-Constructed Cultivation Base for State Key Laboratory of Processing for non-Ferrous Metal and Featured Materials, MOE Key Laboratory of New Processing Technology for Nonferrous Metals and Materials, College of Materials Science and Engineering, Guilin University of Technology, Guilin 541004, P. R. China

[§]UPR3079 CEMHTI, 1D Avenue de la Recherche Scientifique, 45071 Orléans Cedex2, France

[⊗]Faculté des Sciences, Université d'Orléans, Avenue du Parc Floral, 45067 Orléans Cedex 2, France

[∥]Advanced Photon Source, Argonne National Laboratory, Lemont, Illinois 60439, United States

[⊥]Laboratoire Léon Brillouin, CEA Saclay, F-91191 Gif Sur Yvette, France

[#]Instrumental Analysis and Research Center, Sun Yat-Sen University, Guangzhou 510275, P. R. China

Supporting Information

ABSTRACT: The solubility of Ce in the $La_{1-x}Ce_xSrGa_3O_{7+\delta}$ and $La_{1.54-x}Ce_xSr_{0.46}Ga_3O_{7.27+\delta}$ melilites was investigated, along with the thermal redox stability in air of these melilites and the conductivity variation associated with oxidization of Ce^{3+} into Ce^{4+}. Under CO reducing atmosphere, the La in $LaSrGa_3O_7$ may be completely substituted by Ce to form the $La_{1-x}Ce_xSrGa_3O_{7+\delta}$ solid solution, which is stable in air to ~600 °C when $x \geq 0.6$. On the other side, the $La_{1.54-x}Ce_xSr_{0.46}Ga_3O_{7.27+\delta}$ compositions displayed much lower Ce solubility ($x \leq 0.1$), irrespective of the synthesis atmosphere. In the as-made $La_{1-x}Ce_xSrGa_3O_{7+\delta}$, the conductivity increased with the cerium content, due to the enhanced electronic conduction arising from the 4f electrons in Ce^{3+} cations. At 600 °C, $CeSrGa_3O_{7+\delta}$ showed a conductivity of ~10^{-4} S/cm in air, nearly 4 orders of magnitude higher than that of $LaSrGa_3O_7$. The oxidation of Ce^{3+} into Ce^{4+} in $CeSrGa_3O_{7+\delta}$ slightly reduced the conductivity, and the oxygen excess did not result in apparent increase of oxide ion conduction in $CeSrGa_3O_{7+\delta}$. The Ce doping in air also reduced the interstitial oxide ion conductivity of $La_{1.54}Sr_{0.46}Ga_3O_{7.27}$. Neutron powder diffraction study on $CeSrGa_3O_{7.39}$ composition revealed that the extra oxygen is incorporated in the four-linked GaO_4 polyhedral environment, leading to distorted GaO_5 trigonal bipyramid. The stabilization and low mobility of interstitial oxygen atoms in $CeSrGa_3O_{7+\delta}$, in contrast with those in $La_{1+x}Sr_{1-x}Ga_3O_{7+0.5x}$, may be correlated with the cationic size contraction from the oxidation of Ce^{3+} to Ce^{4+}. These results provide a new comprehensive understanding of the accommodation and conduction mechanism of the oxygen interstitials in the melilite structure.

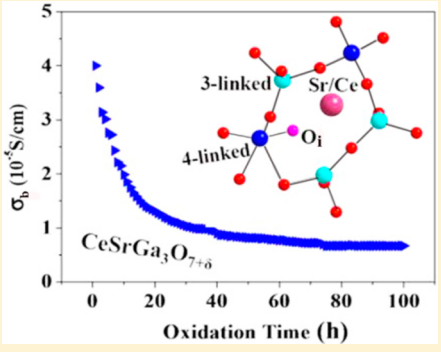

INTRODUCTION

Oxide ion conductors attract considerable attention because of their important applications in energy and catalyst technologies including solid oxide fuel cells (SOFCs), oxygen sensors, oxygen permeation membranes, etc.[1,2] Pure oxide ion conductors with negligible electronic conduction can be used as electrolytes in SOFCs, a promising technology for clean energy conversion with high efficiency and fuel flexibility.[3] The mixed oxide ionic and electronic conductors have potential applications as cathodes in SOFCs, dense membranes for oxygen permeation, and syn-gas production from natural gas. Materials with oxide ion conductivity exceeding 10^{-2} S/cm are required for these various applications,[2,4,5] giving impetus to development of materials with enhanced oxide ion mobility and to understanding of the fundamental mechanism controlling the oxide ion motion at atomic level.

The mobile oxide species are either vacancies or interstitials. In most oxide ion conductors, the charge carriers are oxygen vacancies, and the occurrence of interstitial oxide ion conductors is relatively rare. High-performance electrolytes such as the doped fluorites yttria-stabilized zirconia (YSZ), gadolinium-doped ceria (GDC),[6] and Sr, Mg-doped gallate perovskite $La_{1-x}Sr_xGa_{1-y}Mg_yO_{3-\delta}$ (LSGM)[7,8] are typically oxygen-vacancy-conducting materials. The apatite,[9] scheelite,[10] and melilite[11,12] families are interesting examples of interstitial oxide ion conductors. These materials contain tetrahedral complex anionic units, which are either isolated (apatite and scheelite) or corner-shared in two dimensions (2D) (melilite) with nonbridging terminal oxygen atoms. The variable

Received: July 11, 2014
Published: October 10, 2014

   dx.doi.org/10.1021/ic501662p | Inorg. Chem. 2014, 53, 11589−11597

coordination geometry, rotation, and deformation flexibility of these tetrahedral complex anionic structures have been shown to play key roles in the stabilization and mobility of oxygen interstitials.[1,13]

Among the interstitial oxide ion conductors with tetrahedral structures, the melilite family is of particular interest due to the accommodation and high mobility of oxygen interstitials in their 2D extended tetrahedral network, as evidenced in $La_{1+x}Sr_{1-x}Ga_3O_{7+0.5x}$.[11] The parent phase $LaSrGa_3O_7$, as a competitive phase in LSGM electrolyte,[14] adopts the $A_2B_3O_7$ tetragonal structure of the melilite-type, consisting of alternative eight-coordinated cationic $(La/Sr)_2$ layers and (3,4)-linked tetrahedral Ga_3O_7 layers (the numbers three and four denote that there are two kinds of tetrahedra with three and four bridging oxygen atoms in the structure, respectively) with pentagonal tunnels. $LaSrGa_3O_7$ is an insulator, and replacing Sr^{2+} by La^{3+} introduces excess (interstitial) oxide ions to balance the charge in $La_{1+x}Sr_{1-x}Ga_3O_{7+0.5x}$. These excess anions enter into the pentagonal tunnels at the Ga level along the *c*-axis and between two La/Sr cations, transforming one GaO_4 tetrahedron among the five tetrahedra defining the 5-fold ring into a bipyramidal GaO_5 polyhedron. Single-phase $La_{1.54}Sr_{0.46}Ga_3O_{7.27}$ polycrystalline ceramic reached an impressive 0.02−0.1 S/cm over the 600−900 °C temperature range.[11] The interstitial oxide anions are transported via a hopping mechanism among the pentagonal tunnels in the 2D Ga_3O_7 layers according to a cooperation mechanism involving the rotation and deformation of the tetrahedral framework.[11]

In $La_{1+x}Sr_{1-x}Ga_3O_{7+0.5x}$, oxide ion conductivity increased with the La content (or the oxygen interstitial content) in a nonlinear manner until the interstitial oxide ion ordering occurred when $x > 0.6$, leading to a pseudo-orthorhombic phase and an associated reduced ionic conductivity.[15] In the $Ln_{1+x}Sr_{1-x}Ga_3O_{7+0.5x}$ (Ln = La, Pr, Nd, Sm, Eu, Gd, Dy, Yb, Y) gallate melilite materials, it was found that large lanthanum cationic size favors the stabilization of the oxygen interstitials.[16] The La phase may possess the highest interstitial oxide ion content and ionic conductivity, whereas no oxygen-excess phase was obtained for the Ln = Yb and Y materials. Liu et al. compared the conductivities of $Ln_{1+x}Sr_{1-x}Ga_3O_{7.05}$ ceramics (Ln = La, Pr; x = 0.1, 0.2) and found that the Pr-based materials possessed higher conductivity.[16] This phenomenon was ascribed to the partial oxidation of Pr^{3+} into Pr^{4+} and the existence of 4f electrons in Pr^{3+} cation, which may enhance both the electronic and interstitial oxide ionic conductivities. A similar trend was also observed in the mixed electronic and interstitial oxide ionic conducting $CeNbO_{4+\delta}$ scheelite[17,18] and $LnNi_{0.8}Cu_{0.2}O_{4+x}$ (Ln = La, Pr, Nd) layer perovskite,[19] where the oxidation of Ce^{3+} and Pr^{3+} resulted in a higher oxide ion conductivity.

To address the possibility of enhancing the content and conductivity of oxygen interstitials in $La_{1+x}Sr_{1-x}Ga_3O_{7+0.5x}$ melilites through the Ce substitution and oxidization, we investigated the influence of Ce substitution for La on the structure, conductivity, and thermal stability upon oxidization of $La_{1+x}Sr_{1-x}Ga_3O_{7+0.5x}$ melilites. Here we demonstrate that, instead of promoting the oxide ion conductivity, the Ce^{3+} oxidization to Ce^{4+} causes the localization of oxygen interstitials in the insulating $CeSrGa_3O_{7+\delta}$, which represents a new comprehensive understanding of the accommodation and conduction mechanism of oxygen interstitials in melilite materials.

EXPERIMENTAL SECTION

Polycrystalline samples of $La_{1-x}Ce_xSrGa_3O_{7+\delta}$ ($0 \le x \le 1$) and $La_{1.54-x}Ce_xSr_{0.46}Ga_3O_{7.27+\delta}$ ($0 \le x \le 0.2$) were synthesized from a mixed oxide route using La_2O_3 (99.99%), CeO_2 (99.99%), $SrCO_3$ (99.0+%), and Ga_2O_3 (99.99%) as starting materials. For $La_{1-x}Ce_xSrGa_3O_{7+\delta}$ ($0 \le x \le 1$), stoichiometric starting materials were mixed in an agate mortar using ethanol to disperse the powder. To compensate the volatilization of Ga at high temperatures, small excesses of Ga_2O_3 were required: 1.7 mol % Ga_2O_3 excess for x = 0−0.4, 5% for x = 0.6−0.8, and 6% for x = 1. The dried mixtures were subsequently calcined at 1200 °C for 12 h in air. Then these calcined powders were ground, uniaxially pressed into pellets, and fired at 1350 °C (x = 0, 0.2, 0.4, 0.6, 0.8) or at 1280 °C (x = 1) for 12 h in air (x = 0, 0.2) or in the CO-reducing atmosphere (x = 0.4, 0.6, 0.8, 1.0) produced by the incomplete combustion of carbon powder. To perform neutron powder diffraction measurements, ∼10 g of as-made $CeSrGa_3O_{7+\delta}$ powder were annealed at 525 °C in O_2 flow for 100 h. The preparation of $La_{1.54-x}Ce_xSr_{0.46}Ga_3O_{7.27+\delta}$ ($0 \le x \le 0.2$) is similar to that of $La_{1-x}Ce_xSrGa_3O_{7+\delta}$ ($0 \le x \le 1$): stoichiometric starting materials with 3 mol % excess Ga_2O_3 were first calcined at 1200 °C for 12 h in air, and the ground powders were then uniaxially pressed into pellets and fired at 1350 °C for 12 h in air (x = 0, 0.1) or in the CO reducing atmosphere (x = 0.2). For thermal redox stability investigation, samples of $La_{1-x}Ce_xSrGa_3O_{7+\delta}$ ($0 \le x \le 1$) were annealed for 24 h at each temperature (from 50 to 1000 °C using an interval of 50 °C) in air and then cooled down to room temperature followed by phase examination using X-ray diffraction.

X-ray powder diffraction (XRPD) was performed on a D8 ADVANCE powder diffractometer with Cu Kα radiation. High-quality laboratory XRD data for Rietveld refinement were collected over a 2θ range from 8° to 100° using an interval of 0.02°. Constant-wavelength (λ = 1.225 Å) neutron powder diffraction (NPD) data were collected on the 3T2 diffractometer (Laboratoire Léon Brillouin, France) at a step size of 0.05°. Synchrotron X-ray powder diffraction (SPD) data were collected at ambient temperature on the 11BM diffractometer (λ = 0.413 957 Å) at the Advanced Photon Source (APS), Argonne National Laboratory. Rietveld refinements were performed using Topas Academic software.[20] Bond valence sums (BVSs) were calculated by Brown and Altermatt's method.[21] A JEM-2010HR transmission electron microscope (TEM) instrument operating at 200 kV was used for selected area electron diffraction (SAED) study. Microstructure examination was performed on an FEI Quanta 400 Thermal FE Environment scanning electron microscope (SEM). To determine the oxygen content in $CeSrGa_3O_{7+\delta}$, oxidization thermogravimetric analysis (TGA) was performed under an oxygen flow (20 mL/min) at a heating rate of 10 °C/min from room temperature to 1300 °C using Netzsch STA 449 F3 Jupiter instrument, which was previously calibrated using ZrO_2 as standard material.

Alternating current (AC) impedance spectroscopy (IS) measurements under air and O_2 flow were carried out by using a Solartron1260A impedance/gain-phase analyzer over the 10^{-1}−10^7 Hz range. Prior to the IS measurement, the pellet was coated with platinum or gold paste (depending on the stability temperature of the pellets), which were fired at 800 °C (platinum paste) or 500 °C (gold paste) for 30 min to burn out the organic components to form electrodes.

X-ray photoelectron spectroscopy (XPS) spectra were recorded on a Thermo Fisher Scientific ESCALAB250 Surface Science Instrument spectrometer, under a vacuum of 2×10^{-9} mbar. Monochromatic Al Kα radiation ($h\nu$ = 1486.6 eV) was employed, which was obtained by bombarding the Al anode with an electron gun operating at a beam current of 10 mA and an accelerating voltage of 15 kV. The spectrometer energy scale calibration and the charge correction were made considering that the C 1s signal of the contaminating carbon (C−C or C−H bonds) was centered at 284.8 eV.

RESULTS

Phase Relationship. For the $La_{1-x}Ce_xSrGa_3O_{7+\delta}$ nominal compositions fired in air, single melilite phase can be obtained

dx.doi.org/10.1021/ic501662p | Inorg. Chem. 2014, 53, 11589−11597

for $x < 0.4$ only. For $0.4 \leq x < 1$, CeO_2 was detected as a secondary phase, and in the $x = 1$ composition, no mellilite phase was formed (Supporting Information, Figure S1). Single-phase melilite materials $La_{1-x}Ce_xSrGa_3O_{7+\delta}$ ($0.4 \leq x \leq 1$) could be prepared in the CO-reducing atmosphere. The XRPD patterns of the single-phase $La_{1-x}Ce_xSrGa_3O_{7+\delta}$ ($x = 0$, 0.2, 0.4, 0.6, 0.8, 1.0) melilite solid solution are shown in Figure 1,

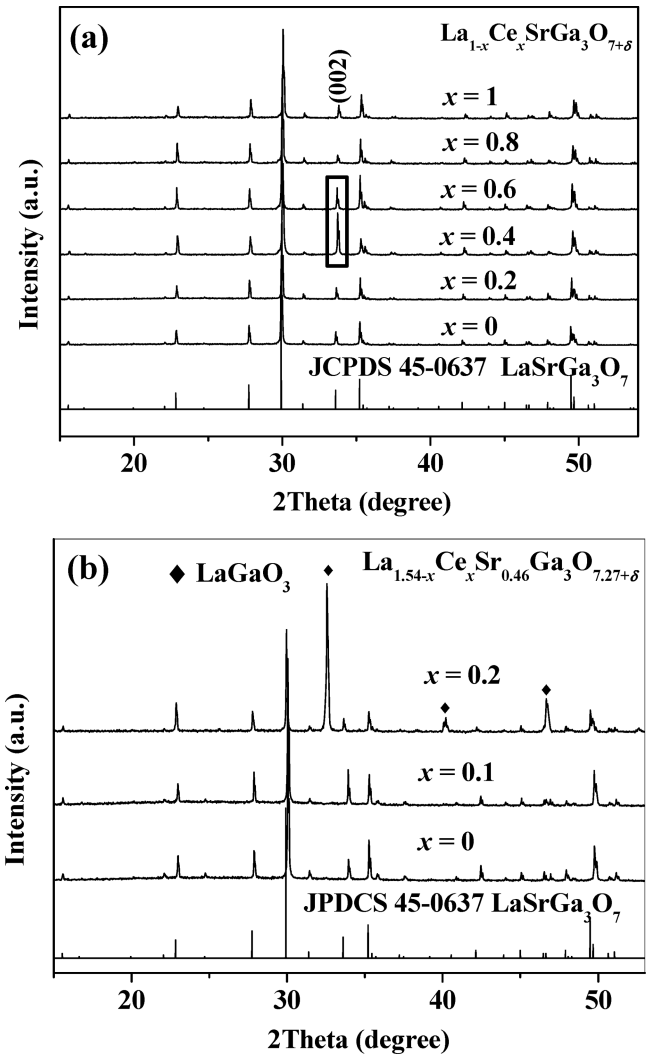

Figure 1. XRD patterns of as-made (a) $La_{1-x}Ce_xSrGa_3O_{7+\delta}$ samples ($x = 0$ and 0.2 were prepared in air, $x = 0.4$–1.0 were prepared in CO) and (b) $La_{1.54-x}Ce_xSr_{0.46}Ga_3O_{7.27+\delta}$ ($x = 0$ and 0.1 were prepared in air, $x = 0.2$ was prepared in CO). The major reflections of the $LaGaO_3$ second phase are labeled in (b).

proving that La in $LaSrGa_3O_7$ can be fully substituted by Ce. The refined lattice parameters of $La_{1-x}Ce_xSrGa_3O_{7+\delta}$ ($0 \leq x \leq 1$) from Rietveld refinements of XRPD data decreased with the Ce content (Supporting Information, Figure S2), obeying Vegard's law. This variation is attributable to the smaller ionic radius of eight-coordinate Ce^{3+}/Ce^{4+} (1.14/0.97 Å) compared with that of La^{3+} (1.16 Å).[22] A preferred orientation on the (002) peak was observed for the sample in the intermediate x range ($x = 0.4$, 0.6), as highlighted in Figure 1a. This may be correlated with the highly plate-shaped textured microstructure in the $La_{0.6}Ce_{0.4}SrGa_3O_{7+\delta}$ sample revealed by SEM experiments (Supporting Information, Figure S3), in contrast to the other compositions showing morphology with randomly orientated grains (Supporting Information, Figure S3). The reason causing such a texture in these two samples remains unclear.

Apart from the Ce substitution in the insulating $LaSrGa_3O_7$, the $La_{1.54-x}Ce_xSr_{0.46}Ga_3O_{7.27+\delta}$ system was prepared not only for investigating the influence of Ce substitution and oxidization on the phase and conductivity of highly interstitial-conducting $La_{1.54}Sr_{0.46}Ga_3O_{7.27}$ composition but also for comparison with $La_{1-x}Ce_xSrGa_3O_{7+\delta}$. For $La_{1.54-x}Ce_xSr_{0.46}Ga_3O_{7.27+\delta}$ fired in air, the Ce content can only be extended to $x = 0.1$, and no apparent change of the cell parameters was observed with the Ce doping. The $LaGaO_3$ perovskite phase was observed for $x \geq 0.2$ (Figure 1b). Firing the $x \geq 0.2$ compositions under the CO reducing atmosphere did not lead to single-phase materials.

Thermal Redox Stability and Electrical Properties. The thermal redox stability in air of the $La_{1-x}Ce_xSrGa_3O_{7+\delta}$ ($x \geq 0.4$) materials prepared in the CO-reducing atmosphere was investigated. The results show that, when $x = 0.4$, the CeO_2 was detected in the product after the sample was annealed at 950 °C for 24 h; when $0.6 \leq x \leq 1$, all the samples decomposed at 650 °C. Alternating current (ac) impedance measurements were carried out for $La_{1-x}Ce_xSrGa_3O_{7+\delta}$ ceramic pellets in air below the decomposition temperature for each material. Table 1 summarizes the densities and the conductivities at 600 °C of

Table 1. Density (ρ) and Bulk Conductivity (σ_b) at 600 °C of $La_{1-x}Ce_xSrGa_3O_{7+\delta}$ Ceramic Pellets

sample	ρ (g/cm^3)	relative density (%)	σ_b at 600 °C (S/cm)
$LaSrGa_3O_{7+\delta}$	4.5(1)	85(2)	$2.32(6) \times 10^{-8}$
$La_{0.8}Ce_{0.2}SrGa_3O_{7+\delta}$	4.49(6)	85(1)	$1.54(2) \times 10^{-6}$
$La_{0.6}Ce_{0.4}SrGa_3O_{7+\delta}$	4.2(2)	79(5)	$4.5(3) \times 10^{-6}$
$La_{0.4}Ce_{0.6}SrGa_3O_{7+\delta}$	4.15(3)	78(1)	$1.56(2) \times 10^{-5}$
$La_{0.2}Ce_{0.8}SrGa_3O_{7+\delta}$	3.57(4)	67(1)	$1.96(2) \times 10^{-5}$
$CeSrGa_3O_{7+\delta}$	3.08(3)	58(1)	$9.6(1) \times 10^{-5}$

the $La_{1-x}Ce_xSrGa_3O_{7+\delta}$ pellets. The Ce-rich compositions ($x = 0.8$, 1) have low densities (~58–67%). Attempts to improve these densities at higher sintering temperature were not successful, owing to the fact that the Ga volatilization under severer reducing atmosphere at higher temperature caused serious phase decomposition. Here the bulk conductivities of $La_{1-x}Ce_xSrGa_3O_{7+\delta}$ are given for comparison in Table 1. Figure 2a shows a typical complex impedance plot of $CeSrGa_3O_{7+\delta}$ measured at 400 °C, which comprises a large and a small semicircular arcs for grain and grain boundary responses, respectively, and small tail with large capacitance of $\sim 10^{-7}$ F/cm at low frequency ascribed to the electrode response,[23] which could be due to the mixed electronic and ionic conduction. Arrhenius plots of the conductivities of $La_{1-x}Ce_xSrGa_3O_{7+\delta}$ (Figure 2b) show that the bulk conductivity increases with the Ce content, and the bulk conductivity of $CeSrGa_3O_{7+\delta}$ at 600 °C is 9.58×10^{-5} S/cm, which is nearly 4 orders of magnitude higher than that of $LaSrGa_3O_7$ (2.32×10^{-8} S/cm). For the $La_{1.54-x}Ce_xSr_{0.46}Ga_3O_{7.27+\delta}$ ($x = 0$, 0.1) materials made in air, the conductivity of $La_{1.44}Ce_{0.1}Sr_{0.46}Ga_3O_{7.27+\delta}$ is lower than that of undoped $La_{1.54}Sr_{0.46}Ga_3O_{7.27}$ above 400 °C (Supporting Information, Figure S4).

Oxidation of Ce and Excess Oxygen in $CeSrGa_3O_{7+\delta}$. To introduce excess oxide ion, which was expected to further improve the oxide ion conductivity as observed in

dx.doi.org/10.1021/ic501662p | Inorg. Chem. 2014, 53, 11589–11597

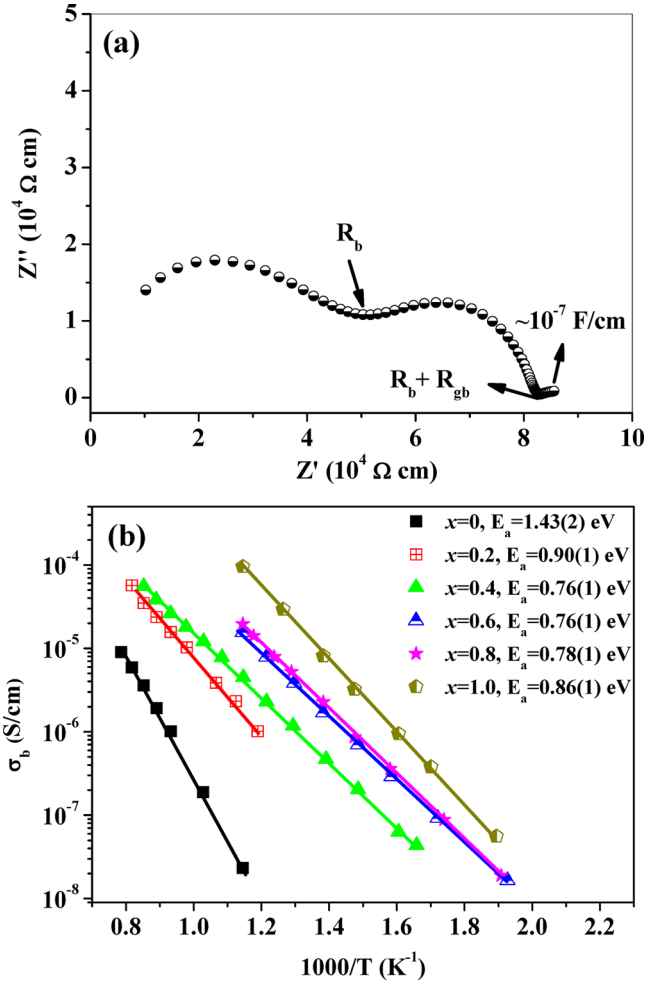

Figure 2. (a) Typical complex impedance plot of as-made $CeSrGa_3O_{7+\delta}$ recorded at 400 °C. R_b and R_{gb} denote bulk and grain boundary resistivities, respectively. (b) Arrhenius plots of bulk conductivities for $La_{1-x}Ce_xSrGa_3O_{7+\delta}$ pellets.

$La_{1+x}Sr_{1-x}Ga_3O_{7+\delta}$, we attempted to extend the Ce/Sr ratio in $Ce_{1+x}Sr_{1-x}Ga_3O_{7+\delta}$. However, for $Ce_{1+x}Sr_{1-x}Ga_3O_{7+\delta}$, no single phase could be obtained even when x = 0.1, as shown in Supporting Information, Figure S5. To examine how the oxidation of Ce affects the conductivity of $CeSrGa_3O_{7+\delta}$, an in situ impedance measurement of $CeSrGa_3O_{7+\delta}$ oxidation was performed under an oxygen flow. The as-prepared $CeSrGa_3O_{7+\delta}$ ceramic pellet painted with gold paste on both surfaces was first fired at 500 °C for 1 h to prepare the electrodes in the $5\%H_2-95\%N_2$ reducing atmosphere flow, avoiding Ce oxidation at this stage. Then the temperature was increased to 525 °C, and the atmosphere was changed to an oxygen flow. The time dependence of electrical resistivity with the oxidation time was monitored, which shows that the conductivity decreased gradually with the oxidation time (Figure 3). After the material was oxidized for 75 h, the conductivity remained constant, indicating that the Ce^{3+} oxidation reached equilibrium. The XRD patterns (Supporting Information, Figure S6) of the powder taken off the ceramic pellet before and after ac impedance measurement both presented pure-melilite phases. The color of the sample before and after oxidation processes changed from grayish to yellow, along with the cell parameters contraction from a = 8.0396(5) to 8.0194(2) Å and from c = 5.3078(2) to 5.2346(1) Å, consistent with the oxidation of Ce^{3+} to smaller Ce^{4+}.[22]

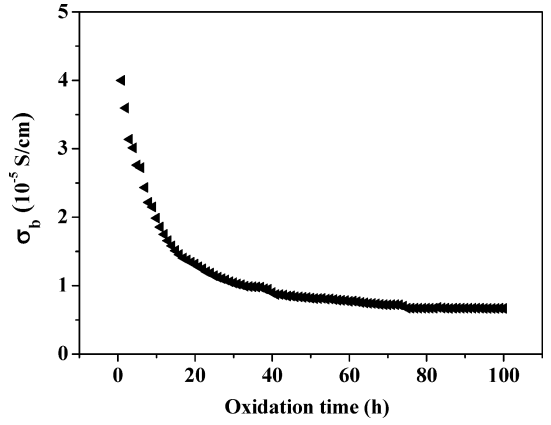

Figure 3. Bulk conductivity at 525 °C of $CeSrGa_3O_{7+\delta}$ as a function of oxidation time under an oxygen flow.

TGA measurement was used to analyze the oxygen content in $CeSrGa_3O_{7+\delta}$. For the as-made $CeSrGa_3O_{7+\delta}$ sample, the TGA data recorded in an O_2 flow shows that the mass increased by 1.29(3)% when the temperature increased from ambient temperature to 1000 °C and then remained constant above 1000 °C (Figure 4). XRPD analysis showed that the final product after the oxidation TGA measurement contains three crystalline phases: CeO_2, $SrGa_2O_4$, and $SrGa_4O_7$, identical to the product of $CeSrGa_3O_{7+\delta}$ prepared at 1280 °C in air. Assuming that all the Ce in the final product is Ce^{4+}, the oxygen content can be calculated using the mass gain from oxidation of Ce^{3+} to Ce^{4+}. The calculated δ in the as-prepared $CeSrGa_3O_{7+\delta}$ is ~0.05(1), corresponding to ~12% of Ce being oxidized to Ce^{4+} in the as-made sample. The oxidation TGA measurement on the oxidized $CeSrGa_3O_{7+\delta}$ powder sample that was annealed in O_2 atmosphere at 525 °C for 100 h and used for the NPD study showed only ~0.3% mass gain during the oxidation measurement. This mass gain led to δ = 0.39(1) for the oxidized sample (Figure 4), corresponding to ~80% of Ce being Ce^{4+} in the sample annealed in O_2 at 525 °C for 100 h.

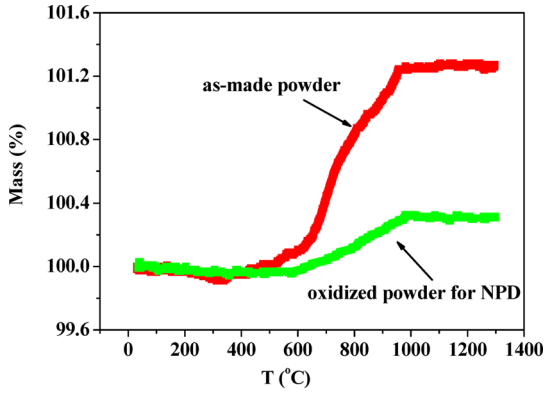

Figure 4. Oxidation TG curves of the as-made $CeSrGa_3O_{7+\delta}$ powder and the oxidized $CeSrGa_3O_{7+\delta}$ (525 °C for 100 h) powder used for the NPD measurement.

XPS experiments were performed to examine the valence of Ce[24−27] in the $CeSrGa_3O_{7+\delta}$ samples. Figure 5 shows the XPS spectra of the as-made $CeSrGa_3O_{7+\delta}$ and the O_2-annealed (525 °C for 100 h) $CeSrGa_3O_{7+\delta}$ powder samples. Both spectra

dx.doi.org/10.1021/ic501662p | Inorg. Chem. 2014, 53, 11589−11597

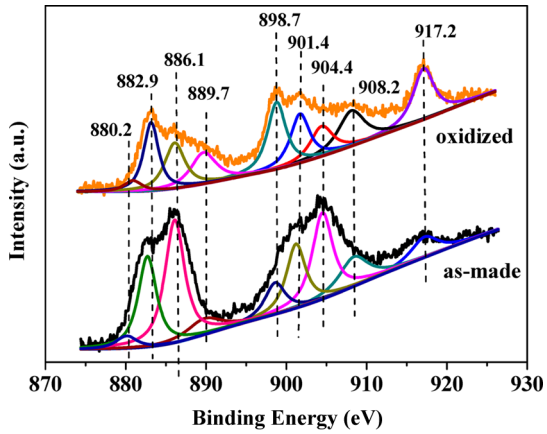

Figure 5. XPS spectra of the as-made and O_2-annealed (at 525 °C for 100 h) $CeSrGa_3O_{7+\delta}$ powders.

show existence of mixed Ce^{3+} and Ce^{4+} in the samples and can be deconvoluted into nine peaks. According to the literature,[27−29] the peaks near 917.2, 908.2, 901.4, 889.7, and 882.9 eV can be ascribed to Ce^{4+}; while the peaks at 904.4 eV, 886.1, and 880.2 eV can be ascribed to Ce^{3+}; the peak at 898.7 eV is assigned to both Ce^{3+} and Ce^{4+}. The XPS spectra confirmed the enhanced Ce^{4+} content in the oxidized $CeSrGa_3O_{7+\delta}$ powder.

Structural Analysis of $CeSrGa_3O_{7+\delta}$. Neutron diffraction data were used to characterize the defect structure in the oxidized $CeSrGa_3O_{7.39}$ sample and establish its linkage with the electrical behavior of $CeSrGa_3O_{7+\delta}$ materials. Electron diffraction (ED) patterns (Supporting Information, Figure S7) confirm that $CeSrGa_3O_{7.39}$ adopts the simple tetragonal melilite cell with space group $P\bar{4}2_1m$. No sign of any local ordering such as extra reflections or streaks could be detected. Preliminary Rietveld refinement of $CeSrGa_3O_{7.39}$ was performed on combined NPD and SPD data based on the parent $LaSrGa_3O_7$ structural model[30] containing one Ce/Sr site (4e), two tetrahedral Ga sites (four-linked Ga1 (2a) and three-linked Ga2 (4e)), and three oxygen sites (bridging O1, terminal O2 and bridging O3), without inclusion of interstitial oxide ions, which gave reliability factors $R_{wp} \approx 3.79\%$, $R_B \approx 3.23\%$ on the NPD data and $R_{wp} \approx 12.7\%$, $R_B \approx 8.55\%$ on the SPD data. Refinement of anisotropic displacement parameters (ADPs) for all the framework atoms significantly improved the fit (R_{wp} = 2.87% on the NPD data and 10.5% on the SPD data). The shape and size of the ellipsoids for the framework atoms (Figure 6) suggest positional disorder.

An extra oxygen site O4 was then randomly added into the refinement to take into account the oxidization of Ce^{3+} to Ce^{4+} in $CeSrGa_3O_{7.39}$. A combined simulated annealing method and Rietveld refinement, which has been proved reliable and successful on determining complex structures from powder diffraction data,[31−34] was applied to refine the position and occupancy for the O4 site over the whole cell. This led to an 8f site (~0.32, ~0.60, ~0.70) with a 0.094(1) occupancy for O4, giving an extra oxygen content of 0.376(4) per $CeSrGa_3O_7$ formula, in good agreement with the composition obtained from TGA measurements. Taking into account the O4 site in the refinement, the fit was notably improved (R_{wp} = 2.58% (NPD) and 10.3% (SPD)). The interstitial oxygen atoms O4 are located within the pentagonal tunnels (Figure 7a) but lie at the framework oxygen level along the *c*-axis (Figure 7b), in contrast to $La_{1+x}Sr_{1-x}Ga_3O_{7+0.5x}$, where the oxygen interstitials

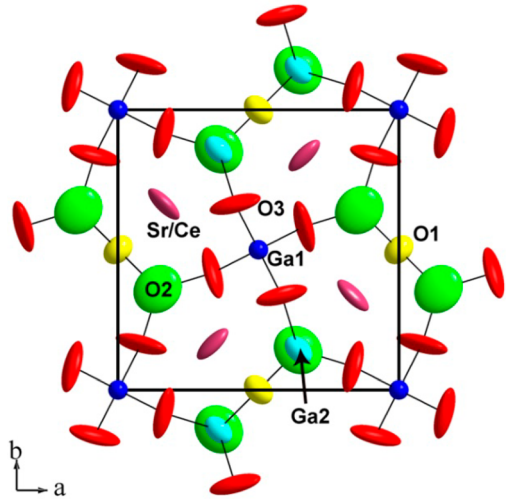

Figure 6. Ellipsoid plot of refined structure of $CeSrGa_3O_{7.39}$ without inclusion of interstitial oxide ions along [001] direction. Thermal ellipsoids are drawn at the 80% probability level.

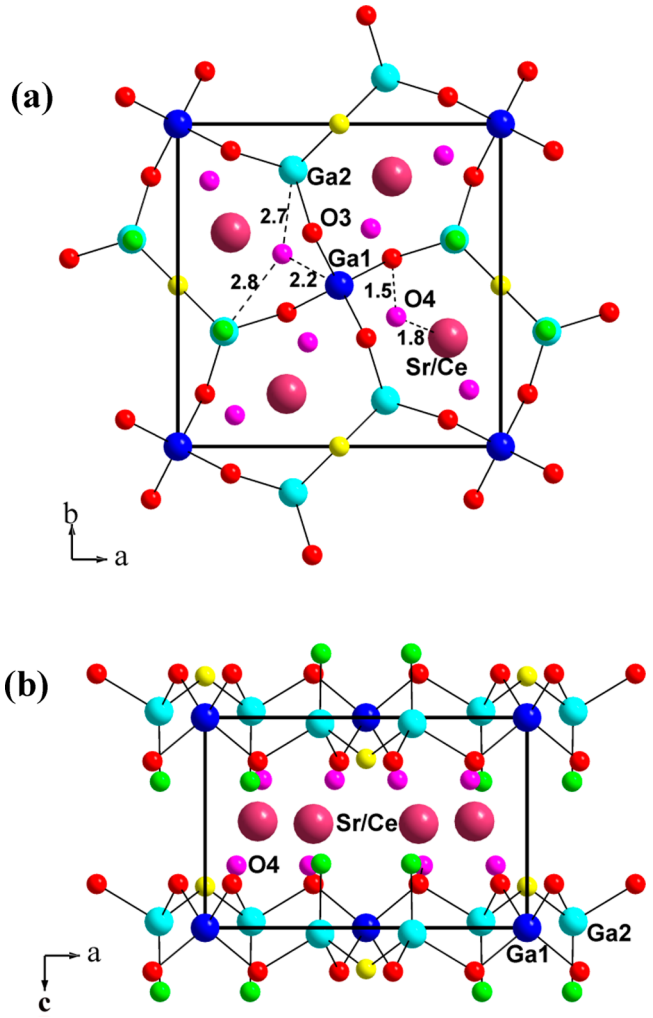

Figure 7. (001) (a) and (010) (b) views of the refined average structure for $CeSrGa_3O_{7.39}$ showing the partially occupied interstitial oxide ion positions (in purple). The numbers in (a) denote the interatomic distances (Å) of O4 with the three neighboring Ga atoms and the short contacts with the framework oxygen O3 and Sr/Ce cation.

dx.doi.org/10.1021/ic501662p | *Inorg. Chem.* 2014, 53, 11589−11597

Table 2. Final Refined Structural Parameters for the Site-Split Model[a] of $CeSrGa_3O_{7.39}$

atom	site	x	y	Z	occupancy	B_{iso} (Å^2)
Ce1/Sr1	8f	0.3495(1)	0.1760(1)	0.5090(2)	0.2265(4)Ce/0.2265(4)Sr	1.45(2)
$(Ce1/Sr1)_L$	8f	0.396(1)	0.227(1)	0.479(3)	0.0235(4)Ce/0.0235(4)Sr	1.45(2)
Ga1	2a	0	0	0	0.906(1)	0.95(1)
$(Ga1)_L$	8f	0.052(2)	−0.025(4)	−0.061(3)	0.0235(4)	0.95(1)
Ga2	4e	0.14320(6)	0.35681(6)	0.9733(2)	1	2.37(1)
O1	2c	0.5	0	0.1942(3)	1	2.37(3)
O21	8f	0.1800(5)	0.3576(4)	0.2986(5)	0.25	2.05(3)
O22	8f	0.1389(4)	0.4061(4)	0.3096(6)	0.25	2.05(3)
O3	8f	0.0787(1)	0.1638(1)	0.7805(2)	0.906(1)	3.45(2)[b]
$(O3)_L$	8f	0.1942(8)	0.1491(9)	0.853(1)	0.094(1)	0.7(1)
O4	8f	0.3169(9)	0.600(1)	0.704(1)	0.094(1)	1.5(1)

[a] a = 8.02391(4) Å; c = 5.23602(3) Å, space group: $P\bar{4}2_1m$, Z = 2; reliability factors: $R_{wp} \approx 2.80\%$, $R_B \approx 1.92\%$ on the NPD data; $R_{wp} \approx 9.47\%$, $R_B \approx 5.50\%$ on the SPD data. [b] The refined anisotropic displacement parameters of O3 are U_{11} = 0.0597(6) Å^2, U_{22} = 0.0353(5) Å^2, U_{33} = 0.0435(6) Å^2, U_{12} = −0.0123(5) Å^2, U_{13} = 0.0063(5) Å^2, U_{23} = 0.0042(5) Å^2; the ellipsoid of O3 displays less elongation along the direction perpendicular to the Ga1−Ga2 line than that (Figure 6) in the average structure model.

were found to lie within the Ga^{3+} cationic plane and close to centers of the pentagonal tunnels.[11,31] The O4 site has an ∼2.2 Å distance to the four-linked tetrahedral center Ga1 and two longer distances (∼2.7−2.8 Å) to the two neighboring three-linked tetrahedral centers Ga2, implying that the interstitial oxygen atoms may be considered as part of the coordinate geometry of the Ga1 tetrahedra. Apart from this, there are two short contacts (∼1.5−1.8 Å) of O4 with one framework O3 atom and one Ce/Sr atom in the tunnel (Figure 7a), coinciding with their significant ADPs: as shown in Figure 6, the O3 ellipsoid displays elongation along the direction perpendicular to the Ga1−Ga2 line, while the Ce/Sr ellipsoid shows elongation within the *ab* plane along the diagonal line in the square formed by the four Ce/Sr atoms in the unit cell. These ADPs reveal the local displacements of O3 (toward the neighboring tunnel) and Ce/Sr (off-center of the tunnel) atoms away from the oxygen interstitial to relieve the short contacts. The interstitial O4 has a slightly shorter contact (∼2.1 Å) with O2, which displays a flattened shape of the ellipsoid (in Figure 6) spreading within the *ab* plane, suggesting disorder within the *ab* plane for the O2 atoms. The O4 has a large separation (∼2.6 Å) from O1, which may leave the O1 site unaffected by the presence of interstitial O4, consistent with the smaller and more isotropic displacement factor for O1.

To model the local relaxation for accommodating the oxygen interstitials, a site-split model was refined for getting chemically sensible environment around oxygen interstitials. Initially the site-split model involved that Ce/Sr and O3 species neighboring O4 are partially displaced away from O4 atoms to $(Ce/Sr)_L$ and $(O3)_L$ sites according to their ADPs (in Figure 6) and the occupancy of O4. General 8f sites were employed for the bulk Ce/Sr and the local $(Ce/Sr)_L$ sites in the site-split model to reduce their atomic displacement parameters and enlarge the interatomic distance between $(Ce/Sr)_L$ and O4. The refinement shows that the local displacements of Ce/Sr and O3 effectively enlarge their interatomic distances with the interstitial O4 to reasonable values of ∼2.2 and ∼2.5 Å, respectively but lead to an under-bonded O4 (BVS ≈ 1.0). At the next stage, the four-linked tetrahedral Ga1 site was partially displaced toward O4 interstitials to $(Gal)_L$ site in the structural model, which resulted in a shorter bond length of $(Ga1)_L$-O4−1.81 Å and thus increased the BVS of O4 to a more satisfactory value of ∼1.7. Note that the original O3 atom framework, corresponding to the bulk structure without interstitial defects in the refined site-split model, still has large atomic isotropic displacement factor (∼3.5 Å^2). A similar case was also found on the O2 site: using a general 8f site for the O2 did not reduce the isotropic displacement factor significantly, and partially displacing the O2 away from the interstitial O4 is not helpful on reducing its isotropic displacement factor. Finally splitting O2 site into two 8f sites (O21 and O22 in Table 2) with half occupancy for each site is effective to reduce its displacement factor (∼2.0 Å^2), and one (O22) of these two sites affords a sensible distance ∼2.5 Å with the interstitial O4, meaning locally O4 site neighbors O22 in the defect structure. Lowering the symmetry was found to be not helpful on reducing the displacement factors of O3 and O2. The final refined structural parameters and interatomic distances in the site-split model of $CeSrGa_3O_{7.39}$ are provided in Table 2 and Supporting Information, Table S1, respectively. The existence of a small amount of CeO_2 phase (∼0.9 wt %) was clearly observed in the SPD data. Such a low amount of the minor phase was poorly discerned in the NPD and laboratory XRD data with lower signal-to-noise ratios. The minor phase was then added into the combined Rietveld refinement. Figure 8 shows the Rietveld plots of NPD and SPD data.

DISCUSSION

As the cerium cations were mainly Ce^{3+} species in the as-made sample, the much higher conductivity of $CeSrGa_3O_{7+\delta}$ than $LaSrGa_3O_7$ is therefore ascribed to the enhanced electronic conductivity arising from 4f electrons in Ce^{3+} cations. Although the TGA (Figure 4) and XPS (Figure 5) data revealed that the oxygen excess (i.e., oxygen interstitial) content was enhanced upon the Ce oxidation in $CeSrGa_3O_{7+\delta}$, the conductivity of $CeSrGa_3O_{7+\delta}$ decreased during the oxidation of Ce^{3+} (Figure 3). This is unlike the $CeNbO_{4+x}$[18] case but consistent with the reduced electronic conductivity owing to the reduced 4f electrons, suggesting that in $CeSrGa_3O_{7+\delta}$ the mobility of the interstitial oxide ions from the oxidation is limited. In other words, the interstitial oxygen atoms are localized in $CeSrGa_3O_{7+\delta}$ and show a low mobility. For the $La_{1.54-x}Ce_xSr_{0.46}Ga_3O_{7+\delta}$ (x = 0.1) material, TGA and XPS measurements are not sufficiently sensitive to analyze the valence of Ce owing to the small amount of cerium in the material. The lower conductivity of the $La_{1.54-x}Ce_xSr_{0.46}Ga_3O_{7.27+\delta}$ (x = 0.1) material prepared in air than that of the undoped $La_{1.54}Sr_{0.46}Ga_3O_{7.27}$ (Supporting

dx.doi.org/10.1021/ic501662p | Inorg. Chem. 2014, 53, 11589−11597

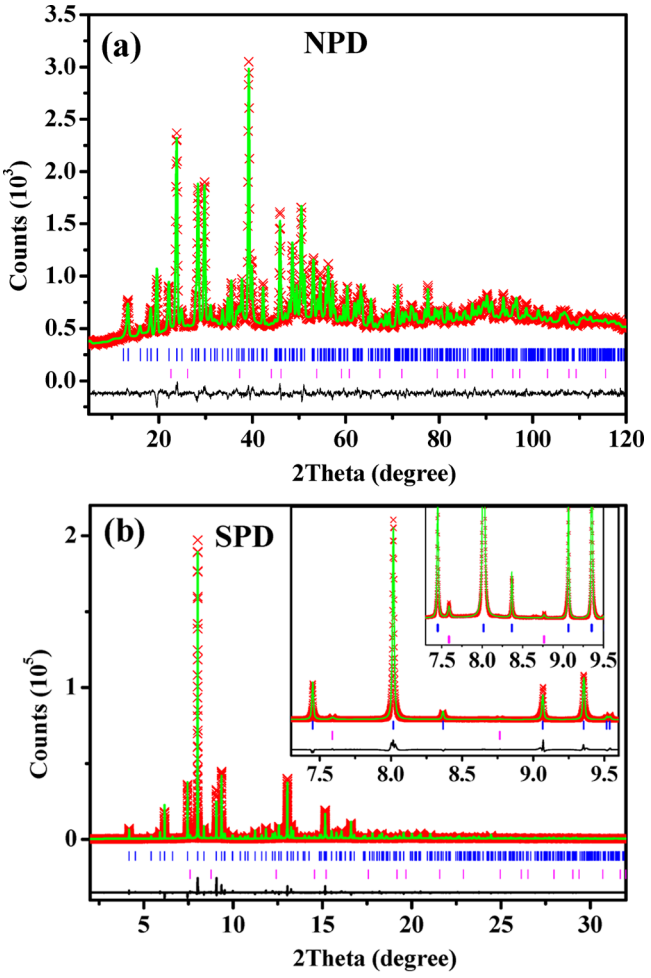

Figure 8. Rietveld plots of NPD (a) and SPD (b) data for $CeSrGa_3O_{7.39}$. The inset in (b) enlarges the fit in the 7.3−9.6° 2Theta range with an additional plot for enlarging the reflections from the impurity CeO_2. Blue and pink ticks indicated Bragg reflection positions of $CeSrGa_3O_{7.39}$ and CeO_2, respectively.

Information, Figure S4) is indicative of Ce^{4+} as a dominant valence for Ce cations in the $x = 0.1$ composition prepared in air. Otherwise higher conductivity would have been observed on $La_{1.54-x}Ce_xSr_{0.46}Ga_3O_{7+\delta}$ ($x = 0.1$) given that the 4f electrons in Ce^{3+} would enhance the electron conductivity. Therefore, the conductivity behavior of $La_{1.54-x}Ce_xSr_{0.46}Ga_3O_{7.27+\delta}$ reproduced the localization of oxygen interstitials in $CeSrGa_3O_{7+\delta}$.

Figure 9a,b represents pentagonal tunnels with and without interstitial defects in $CeSrGa_3O_{7.39}$. Ce^{3+} oxidization leads to the incorporation of oxygen interstitials into the oxygen framework (Figure 7b) along the *c*-axis, which displaces local $(O3)_L$ and $(Sr1/Ce1)_L$ atoms away from the interstices: $(Sr1/Ce1)_L$ atom is off-center of the pentagonal tunnel, and $(O3)_L$ is displaced toward the neighboring tunnel free of oxygen interstitial. The oxygen interstitial enters into a four-linked $Ga1O_4$ bonding environment and transforms it into a distorted five-coordinate trigonal bipyramid (Figure 9c). Similar GaO_5 geometry has been observed in $La_{1+x}A_{1-x}Ga_3O_{7+0.5x}$ (A = Sr, Ca),[11,32,35,36] $Ga_2Te_4O_{11}$,[37] and $NaGa_2(OH)(PO_4)_2$.[38] The stabilization of interstitial oxygen in $CeSrGa_3O_{7.39}$ is different from that observed in the $La_{1+x}A_{1-x}Ga_3O_{7+0.5x}$ (A = Sr, Ca)[11,32,35,36] melilites. Rosseinsky et al. proposed from neutron diffraction data that the excess oxygen in $La_{1+x}A_{1-x}Ga_3O_{7+0.5x}$ materials is located within the pentagonal tunnel at approximately the same level as the Ga layer along the *c*-axis and enters into the environment of one of the three-linked GaO_4 tetrahedra, which changes to a trigonal bipyramid GaO_5,[11] as shown in Figure 9d. In the interstitial-conducting $La_{1.54}Sr_{0.46}Ga_3O_{7.27}$, the La/Sr atoms are locally displaced along the tunnel direction (i.e., the *c*-axis) toward interstitials to contribute to stabilizing the interstitials,[11] which is in contrast with the off-center local displacement in the tunnel for Sr/Ce away from interstitial within the *ab* plane identified in this study. Latterly, atomistic simulation[35] and pair-distribution function analysis[36] have shown another possibility: the interstitial oxygen could be shifted off the center of the pentagonal tunnel, forming bonds with two three-linked Ga2 atoms and one four-linked Ga1 atom (Figure 9e). The existence of terminal oxygen atoms in three-linked Ga tetrahedra affords rotation and deformation flexibility to the tetrahedral framework, which may cooperate on the migration of oxygen interstitials within the tetrahedral layers. The great contrast between the stabilization and mobility of $CeSrGa_3O_{7+\delta}$ and $La_{1+x}A_{1-x}Ga_3O_{7+0.5x}$ may emphasize that bonding of the three-linked Ga centers with the terminal oxygen atoms is the key factor for controlling the mobility of oxygen interstitials in gallate melilites. In $CeSrGa_3O_{7.39}$, the four-linked GaO_4 with all oxygen atoms as bridging atoms has constrained deformation and rotation, which is unfavorable for transporting the bonded interstitials and thus limits the mobility of the oxygen interstitials, as revealed by the insulating electrical property of $CeSrGa_3O_{7+\delta}$.

The localization of oxygen interstitials in $CeSrGa_3O_{7+\delta}$ may also be attributed to the oxidation of Ce^{3+} into Ce^{4+} as the origin of this oxygen excess occurs simultaneously with the A-cationic size contraction: Ce^{4+} has a smaller ionic radius (0.97 Å in eight-coordination) than Ce^{3+} (1.143 Å). The eight-coordinate cage in the melilite structure is relatively large for the small Ce^{4+}, and the location of interstitial oxygen at the level of the oxygen framework affords an extra and short bond (~2.2 Å in Supporting Information, Table S1) to contribute to stabilization of Ce^{4+}. On the other hand, as one interstitial oxygen atom requires the formation of two Ce^{4+} cations ($2\ Ce^{3+} + 1/2\ O_2 \rightarrow 2\ Ce^{4+} + O^{2-}$), in addition to the incorporation of oxygen interstitials, the local structure is even more complicated by the distortion of the tetrahedral framework for shortening the bond lengths of Ce^{4+} with oxygen atoms to meet the bonding environments for all of the smaller Ce^{4+} cations, which the site-split model (in Table 1) is not able to fully describe. Such distortion of tetrahedral framework contributes to the positional disorder in $CeSrGa_3O_{7+\delta}$, as suggested by the large atomic displacements for O3 and O2 in the site-split model refinement. Therefore, the complex disordered structural behavior observed in $CeSrGa_3O_{7+\delta}$ is associated with structural relaxation for not only accommodating the excess oxygen but also adapting the cationic contraction in the tunnels induced by the oxidization of Ce^{3+} to Ce^{4+}. The distortion of tetrahedral framework in $CeSrGa_3O_{7+\delta}$ may not allow the oxygen interstitials to be stabilized in the pentagonal tunnels at the gallium cationic level as observed in $La_{1+x}A_{1-x}Ga_3O_{7+0.5x}$. The localizing role of the Ce^{4+} cations on the interstitial oxygen atoms coincides with the observation that the Ce-doped $La_{1.54}Sr_{0.46}Ga_3O_{7.27}$ prepared in air has lower conductivity than that of the undoped $La_{1.54}Sr_{0.46}Ga_3O_{7.27}$ composition (Supporting Information, Figure S4).

dx.doi.org/10.1021/ic501662p | *Inorg. Chem.* 2014, 53, 11589−11597

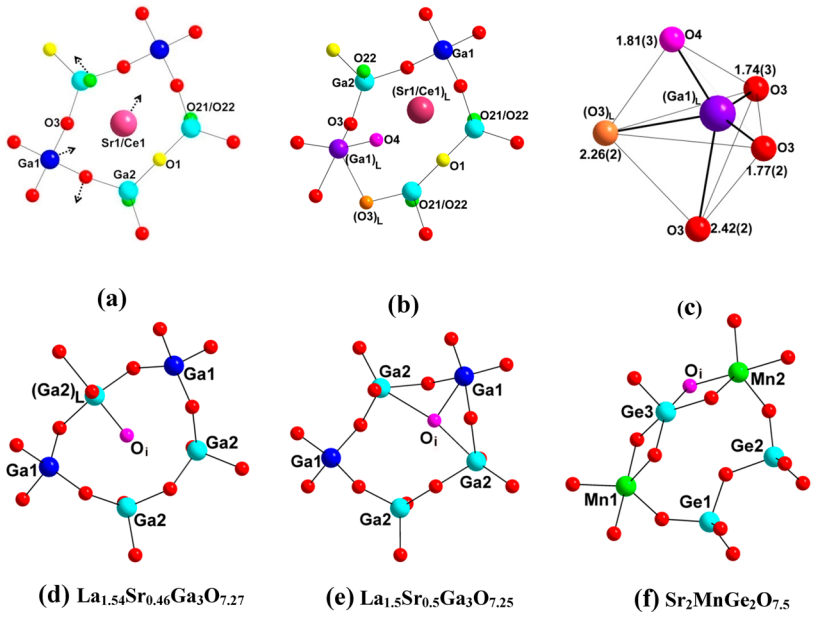

Figure 9. (a) Pentagonal tunnels of the bulk $CeSrGa_3O_{7.39}$ structure without interstitial defect and (b) local defect structure containing interstitial oxygen. The arrows denote the local atomic displacement directions for accommodating the interstitial defects. The interstitial oxygen (purple spheres in (b, c)) transforms one $Ga1O_4$ tetrahedron to a trigonal bipyramid $(Ga1)_LO_5$ (c). Ga−O bond lengths (Å) are given in (c). (d, e, f) The pentagonal tunnels in the local defect structure containing the interstitial oxygen (purple sphere O_i) in $La_{1.54}Sr_{0.46}Ga_3O_{7.27}$ (d and e from the analysis of neutron diffraction data[11] and atomistic simulation (or pair-distribution function analysis),[11,35,36] respectively) and $Sr_2MnGe_2O_{7.5}$[39] (f). In (d−f), all the framework oxygen atoms are plotted in red.

As the melilite structure consists of an AO_8 layer sharing the oxygen atoms with a B_3O_7 tetrahedral layer, it was proposed that the horizontal sizes of two unit blocks should be matching each other to form an energetically stable phase.[39] In the recently reported $Sr_2Mg_{1-x}Mn_xGe_2O_{7+\delta}$ ($0 \le x \le 1$) melilite material,[39] when the Mg^{2+} ions (0.57 Å in four-coordination[22]) were substituted by larger Mn^{2+} ions (0.66 Å),[22] the Mn^{2+} cations were automatically oxidized into smaller Mn^{3+} (0.58 Å in five-coordination,[22] close to that of Mg^{2+}) to avoid the mismatch induced by the $Mn^{2+}O_4$−GeO_4 layer to the SrO_8 layer. The excess oxide ions resulting from the oxidation of Mn^{2+} to Mn^{3+} in $Sr_2MnGe_2O_{7.5}$ were found to lie also at the framework oxygen level (which is similar to the $CeSrGa_3O_{7+\delta}$ case here) and to be involved in the bonding environments of both three-linked Ge^{4+} and four-linked Mn^{3+} centers, which transform the corner-shared MnO_4−GeO_4−MnO_4 unit into the edge-shared MnO_5−GeO_5−MnO_5 unit (in Figure 9f), where GeO_5 and MnO_5 are, respectively, a square pyramid and a trigonal bipyramid. The stabilization of the oxygen interstitials in $Ln_{1+x}Sr_{1-x}Ga_3O_{7+\delta}$ (Ln = La, Pr, Nd, Sm, Eu, Gd, Dy, Yb, Y)[16] is favored by the large lanthanum cationic size and may also be attributable to the interlayer size match factor. Indeed, among the $LnSrGa_3O_7$ series, the $LaSrGa_3O_7$ may present the best interlayer size match, which may be slightly altered by the La substitution for Sr and thus stabilizing the optimal interstitial oxygen content. As a consequence, the substitution of smaller lanthanum cation for Sr could deteriorate the interlayer size mismatch, rendering it difficult to extend the Ln/Sr ratio. In the case of $CeSrGa_3O_7$, Ce^{3+} has an ionic radius similar to La^{3+} (1.16 Å). When Ce^{3+} is oxidized into Ce^{4+} (0.97 Å), which is about 15% smaller, a considerable interlayer size mismatch between the $(Ce/Sr)O_8$ layer and Ga_3O_7 layer is induced, which may account for the instability of this material in air at high temperature.

CONCLUSION

In $LaSrGa_3O_7$, lanthanum can be substituted with cerium in the CO-reducing atmosphere to form the $La_{1-x}Ce_xSrGa_3O_{7+\delta}$ ($0 \le x \le 1$) solid solution, which decomposed at temperatures ≥650 °C in air when $x \ge 0.6$. The conductivities of $La_{1-x}Ce_xSrGa_3O_{7+\delta}$ increased with the Ce content, mainly owing to the enhanced electronic conduction from 4f electrons in Ce^{3+}. Oxidation from Ce^{3+} to Ce^{4+} in $CeSrGa_3O_{7+\delta}$ introduced mobility-limited interstitial oxide ions, thus decreasing the total conductivity. The NPD data analysis revealed that the excess oxygen is localized at the framework oxygen level along the *c*-axis via incorporation into the coordination environment of a four-linked GaO_4 tetrahedron, which then turns into a distorted GaO_5 bipyramid and constrains the mobility of oxygen interstitials. Comparison with the other melilite structures containing oxygen interstitials led to understanding the role of the contraction on the A-cationic size, caused by the oxidation of Ce^{3+} to smaller Ce^{4+}, on localizing the interstitial oxygen atoms and affecting the phase instability of $La_{1-x}Ce_xSrGa_3O_{7+\delta}$ ($0.4 \le x \le 1$) at high temperature. The localization of oxygen interstitials by Ce^{4+} was further evidenced by the reduced conductivity of $La_{1.44}Ce_{0.1}Sr_{0.46}Ga_3O_{7.27+\delta}$ compared with that of $La_{1.54}Sr_{0.46}Ga_3O_{7.27}$.

ASSOCIATED CONTENT

Supporting Information

XRD patterns of the nominal $CeSrGa_3O_{7+\delta}$ composition prepared in air; refined cell parameters of as-made $La_{1-x}Ce_xSrGa_3O_{7+\delta}$; SEM pictures of $La_{0.6}Ce_{0.4}SrGa_3O_{7+\delta}$ and as-made $CeSrGa_3O_{7+\delta}$; conductivity of $La_{1.54-x}Ce_xSr_{0.46}Ga_3O_{7.27+\delta}$ (x = 0, 0.1); XRD patterns of $Ce_{1+x}Sr_{1-x}Ga_3O_{7+\delta}$ (x = 0, 0.1); XRD patterns of as made and low-temperature O_2-annealed $CeSrGa_3O_{7+\delta}$; ED patterns of

dx.doi.org/10.1021/ic501662p | Inorg. Chem. 2014, 53, 11589−11597

$CeSrGa_3O_{7.39}$; interatomic distances in the site-split model of $CeSrGa_3O_{7.39}$; crystallographic information file in CIF format of $CeSrGa_3O_{7.39}$ in the site-split model. This material is available free of charge via the Internet at http://pubs.acs.org/.

AUTHOR INFORMATION

Corresponding Authors

*E-mail: kuangxj@glut.edu.cn. (X.K.)
*E-mail: ceswmm@mail.sysu.edu.cn. (M.W.)

Notes

The authors declare no competing financial interest.

ACKNOWLEDGMENTS

This work is funded by National Science Foundation of China (No. 21101174), the Research Project (No. 213030A) of Chinese Ministry of Education, Program for New Century Excellent Talents in University (No. NCET-13-0752), and the Guangdong Province Research Project for industrial applications (Nos. 2012B09000026 and 2011A090200083). Use of the Advanced Photon Source (beamline 11-BM) at Argonne National Laboratory was supported by the U.S. Department of Energy under Contract No. DE-AC02-06CH11357. The authors acknowledge the support of the Laboratoire Léon Brillouin at CEA/Saclay (beamline 3T2) for the neutron beamtime. X.K. also thanks Guilin University of Technology and Chinese Ministry of Education Scientific Research Foundation for Returned Scholars for the Start-up Funds. We thank Prof. C.-Y. Su for access to TGA instrument and Ms. H.-J. Yu for helping with the TGA measurement.

REFERENCES

(1) Kuang, X.; Payne, J. L.; Johnson, M. R.; Radosavljevic Evans, I. *Angew. Chem., Int. Ed* **2012**, *51*, 690−694.
(2) Steele, B. C. H.; Heinzel, A. *Nature* **2001**, *414*, 345−352.
(3) Kishimoto, M.; Iwai, H.; Miyawaki, K.; Saito, M.; Yoshida, H. *J. Power Sources* **2013**, *223*, 268−276.
(4) Goodenough, J. B. *Annu. Rev. Mater. Res.* **2003**, *33*, 91−128.
(5) Boivin, J. C.; Mairesse, G. *Chem. Mater.* **1998**, *10*, 2870−2888.
(6) Minh, N. Q. *J. Am. Ceram. Soc.* **1993**, *76*, 563−588.
(7) Huang, P.; Petric, A. *J. Electrochem. Soc.* **1996**, *143*, 1644−1648.
(8) Huang, K.; Tichy, R. S.; Goodenough, J. B. *J. Am. Ceram. Soc.* **1998**, *81*, 2565−2575.
(9) Leon-Reina, L.; Losilla, E. R.; Martinez-Lara, M.; Bruque, S.; Aranda, M. A. G. *J. Mater. Chem.* **2004**, *14*, 1142−1149.
(10) Esaka, T.; Mina-ai, T. *Solid State Ionics* **1992**, *52*, 319−325.
(11) Kuang, X.; Green, M. A.; Niu, H.; Zajdel, P.; Dickinson, C.; Claridge, J. B.; Jantsky, L.; Rosseinsky, M. J. *Nat. Mater.* **2008**, *7*, 498−504.
(12) Rozumek, M.; Majewski, P.; Schluckwerder, H.; Aldinger, F.; Künstler, K.; Tomandl, G. *J. Am. Ceram. Soc.* **2004**, *87*, 1795−1798.
(13) Evans, I. R.; Howard, J. A. K.; Evans, J. S. O. *Chem. Mater.* **2005**, *17*, 4075−4077.
(14) Huang, K. Q.; Tichy, R. S.; Goodenough, J. B. *J. Am. Ceram. Soc.* **1998**, *81*, 2576−2580.
(15) Thomas, C. I.; Kuang, X.; Deng, Z.; Niu, H.; Claridge, J. B.; Rosseinsky, M. J. *Chem. Mater.* **2010**, *22*, 2510−2516.
(16) Liu, B.; Ding, D.; Liu, Z.; Chen, F.; Xia, C. *Solid State Ionics* **2011**, *191*, 68−72.
(17) Packer, R. J.; Skinner, S. J.; Yaremchenko, A. A.; Tsipis, E. V.; Kharton, V. V.; Patrakeev, M. V.; Bakhteeva, Y. A. *J. Mater. Chem.* **2006**, *16*, 3503−3511.
(18) Packer, R.; Skinner, S. *Adv. Mater.* **2010**, *22*, 1613−1616.
(19) Miyoshi, S.; Furuno, T.; Sangoanruang, O.; Matsumoto, H.; Ishihara, T. *J. Electrochem. Soc.* **2007**, *154*, B57−B62.
(20) Coelho, A. TOPAS Academic Version 4.1; Coelho Software: Brisbane, Australia, 2007.
(21) Brown, I.; Altermatt, D. *Acta Crystallogr., Sect. B* **1985**, *41*, 244−247.
(22) Shannon, R. *Acta Crystallogr., Sect. A* **1976**, *32*, 751−767.
(23) Irvine, J. T. S.; Sinclair, D. C.; West, A. R. *Adv. Mater.* **1990**, *2*, 132−138.
(24) Yao, H.; Yao, Y. F. *J. Catal.* **1984**, *86*, 254−265.
(25) Tschöpe, A.; Ying, J. *Nanostruct. Mater.* **1994**, *4*, 617−623.
(26) Skarman, B.; Grandjean, D.; Benfield, R.; Hinz, A.; Andersson, A.; Wallenberg, L. *J. Catal.* **2002**, *211*, 119−133.
(27) Romeo, M.; Bak, K.; Fallah, J. E.; Normand, F. L.; Hilaire, L. *Surf. Interface Anal.* **1993**, *20*, 508−512.
(28) Patsalas, P.; Logothetidis, S.; Sygellou, L.; Kennou, S. *Phys. Rev. B: Condens. Matter Mater. Phys.* **2003**, *68*, 035104.
(29) Burroughs, P.; Hamnett, A.; Orchard, A. F.; Thornton, G. *J. Chem. Soc., Dalton Trans.* **1976**, 1686.
(30) Skakle, J.; Herd, R. *Powder Diffr.* **1999**, *14*, 195−202.
(31) Cao, J.; Kuang, X.; Allix, M.; Dickinson, C.; Claridge, J. B.; Rosseinsky, M. J.; Iddles, D. M.; Su, Q. *Chem. Mater.* **2011**, *23*, 5058−5067.
(32) Li, M. R.; Kuang, X.; Chong, S. Y.; Xu, Z.; Thomas, C. I.; Niu, H.; Claridge, J. B.; Rosseinsky, M. J. *Angew. Chem., Int. Ed.* **2010**, *49*, 2362−2366.
(33) Evans, I. R.; Howard, J. A.; Evans, J. S. *J. Mater. Chem.* **2003**, *13*, 2098−2103.
(34) Kuang, X.; Li, Y.; Ling, C. D.; Withers, R. L.; Evans, I. R. *Chem. Mater.* **2010**, *22*, 4484−4494.
(35) Tealdi, C.; Mustarelli, P.; Islam, M. S. *Adv. Funct. Mater.* **2010**, *20*, 3874−3880.
(36) Mancini, A.; Tealdi, C.; Malavasi, L. *Int. J. Hydrogen Energy* **2012**, *37*, 8073−8080.
(37) Dutreilh, M.; Thomas, P.; Champarnaud-Mesjard, J. C.; Frit, B. *Solid State Sci.* **2001**, *3*, 423−431.
(38) Guesdon, A.; Monnin, Y.; Raveau, B. *J. Solid State Chem.* **2003**, *172*, 237−242.
(39) Kim, T. G.; Kim, S. J.; Lin, C.; Liu, R.; Chan, T.; Im, S. J. *J. Mater. Chem. C* **2013**, *1*, 5843−5848.